CrystEngComm

Tetranitro- and Tetraamino- dibenzo[18]crown-6-ether Derivatives: Complexes for Alkali Metal Ions, Redox Potentials, Crystal Structures, Molecular Sorption, and Proton Conducting Behaviors.

Journal:	*CrystEngComm*
Manuscript ID	CE-ART-04-2022-000582.R1
Article Type:	Paper
Date Submitted by the Author:	07-Jun-2022
Complete List of Authors:	Shimizu, Yuta; Tohoku University Takeda, Takashi; Tohoku University, Institute of Multidisciplinary Research for Advanced Materials Hoshino, Norihisa; Niigata University, Department of Materials Science and Technology, Faculty of Engineering Akutagawa, Tomoyuki; Tohoku University, Institute of Multidisciplinary Research for Advanced Materials

SCHOLARONE™
Manuscripts

Please do not adjust margins

ARTICLE

Tetranitro- and Tetraamino- dibenzo[18]crown-6-ether Derivatives: Complexes for Alkali Metal Ions, Redox Potentials, Crystal Structures, Molecular Sorption, and Proton Conducting Behaviours

Received 00th January 20xx,
Accepted 00th January 20xx

DOI: 10.1039/x0xx00000x

Yuta Shimizu,[a] Takashi Takeda,[a, b]* Norihisa Hoshino,[a, b] and Tomoyuki Akutagawa [a, b]*

Tetranitro-dibenzo[18]crown-6 (**1**) and tetraamino-dibenzo[18]crown-6 (**2**) are ion-recognition electron acceptor and electron donor molecules, respectively. The electron-accepting ability of **1** is lower than that of *o*-dinitorobenzene, whereas the electron-donating ability of **2** exceeds that of tetrathiafulvelene, a typical electron donor. The oxidation potential of **2** is drastically reduced by di-protonation at the two $-NH_2$ sites under acidic conditions. Thermally annealed **1** exhibits gate-opened gas adsorption–desorption behaviors for CO_2 at 200 K and N_2 at 77 K. The central cavity of **1** can bind alkali metal ions (M) to form M(**1**) complexes for M = Na^+, K^+, Rb^+, and Cs^+; these crystallize into monomers (M = Na^+ and K^+), dimers (M = Rb^+), and one-dimensional polymers (M = Cs^+) in single crystals of [M(**1**)I]·nCH_3CN. Multiple M^+•••O_2N- axial coordination at the M^+ site generates dimer and polymer networks in solids. Single crystals of [Na(**2**)$(H_2SO_4)_3$]·nH_2O and [K(**2**)$(H_2SO_4)_3$]·nH_2O were obtained by crystallization of **2** in the presence of Na^+ and K^+, respectively, in dilute H_2SO_4. The single crystals formed an ionic channel in the one-dimensional array of ••• [$(Na)_{0.25}$(**2**)]•••H_2O•••[$(H_3O)_{0.25}$(**2**)]•••H_2O•••, and the mixed protonated state of HSO_4^- and H_2SO_4 formed an O–H•••O= hydrogen-bonding network with the aid of additional H_2O molecule occupation around the ionic channels. In contrast, the two oxygen atoms of HSO_4^- were axially coordinated to the K(**2**) complex, which isolated them from each other, and HSO_4^- and H_2O occupied [K(**2**)$(H_2SO_4)_3$]. These two hydrated crystals showed a proton conductivity (σ_{H+}) of ~5 μS cm^{-1} at 310 K, while the dehydrated crystals disappeared the σ_{H+} values; furthermore, the motional freedom of the polar HSO_4^- was observed in the Debye-type dielectric relaxations.

Introduction

Cyclic oligo(ethylene glycol) derivatives such as [15]crown-5 and [18]crown-6 can selectively recognize alkali metal ions (M^+) according to their central cavity size.[1-3] This has been applied in ion sensing,[4, 5] ion transport,[6, 7] and catalytic properties.[8] A variety of functional crown ethers have already been prepared for applications in material chemistry. For instance, simple molecules of [15]crown-5 and [18]crown-6 exhibit high Na^+ and K^+ recognition abilities, respectively; here, the multiple electrostatic M^+•••O interactions between M^+ and the lone pairs of oxygen atoms effectively fix the M^+ inside the cavity.[1-3, 10] The selective M^+ recognition ability of crown ethers has been implemented for material designs with various physical properties, including absorption–fluorescence,[11-13] electrical conduction,[14-16] magnetic,[17-20] dielectric,[21, 22] and ferroelectric responses.[23-24]

The physical properties of π-conjugated molecules are dominated by the frontier orbitals of the highest occupied molecular orbital (HOMO) and lowest unoccupied molecular orbital (LUMO) in the solution and solid phases, which can be controlled by the chemical design of the molecule. The redox properties of the electron donor and acceptor are governed by the HOMO and LUMO energy levels, respectively; these are controlled by the introduction of electron-withdrawing and electron-donating substituents to the π-core. The strengths of the electron acceptor and donor are determined using the electron affinity (E_A) and ionization potential (I_P), respectively. For instance, the typical electron acceptors of 7,7,8,8-tetracyano-*p*-quinodimethane (TCNQ) and *p*-benzoquinone (*p*BQ) exhibit electron affinities of 2.90 and 1.91 eV, respectively,[25] while the electron donating abilities of tetrathiafulvalene (TTF) and *p*-phenylendiamine are 6.4 and 6.84 eV, respectively.[27, 28] The conventional chemical design for the introduction of electron-withdrawing groups such as $-NO_2$ and =O groups or electron-donating $-NH_2$ and -OH substituents represents a typical technique used to tune the redox properties of π-molecules. In contrast, the energy stabilization achieved by aromaticity in the oxidation and reduction processes realizes the strong electron donor property of TTF and the acceptor property of TCNQ. In these donor–acceptor systems, the charge transfer and recombination processes

[a] *Graduate School of Engineering, Tohoku University, Sendai 980-8579, Japan.*
[b] *Institute of Multidisciplinary Research for Advanced Materials (IMRAM), Tohoku University, 2-1-1 Katahira, Aoba-ku, Sendai 980-8577, Japan.*
[c] *E-mail: takashi@tohoku.ac.jp and akutagawa@tohoku.ac.jp*
† Footnotes relating to the title and/or authors should appear here.
Electronic Supplementary Information (ESI) available: [details of any supplementary information available should be included here]. See DOI: 10.1039/x0xx00000x

Please do not adjust margins

between the electron-donating and electron-accepting molecules play an important role in the electrical conduction and emission properties of the molecular assembly.[29-31]

Both electron and ion transport processes play an essential role in biological systems, including multiple electron transfer and ionic channels.[32] In addition, fast ionic transport has been observed as an important phenomenon in secondary batteries. Therefore, many ion-conducting materials have been developed for application in such batteries. Recently, the fast Na^+ and Mg^{2+} ionic conducting materials have attracted significant attention for the realization of the next generation secondary batteries instead of the Li^+ ones.[33, 34] Acyclic oligo(ethylene glycole) has been utilized for the solid state Li^+ and Na^+ conducting polymers,[35-37] and a regular array of the central pores of [18]crown-6 can produce ionic channels in the molecular assembly.[14, 15, 38, 39] For instance, the ionic channel of $[(Li^+)_x([18]crown-6)]_\infty$ and $[(Na^+)_x([18]crown-6)]_\infty$ have been introduced into the electrically conductive $[Ni(dmit)_2]$ (dmit = 2-thioxo-1,3-dithiole-4,5-dithiolate) and TCNQ salts as a counter-cation structure to compensate the total charge valance of the crystals.[14, 15, 40-42] The motional freedom of Li^+ and Na^+ in the ionic channels influenced the freedom of conduction electrons on the π-stacking column of $[Ni(dmit)_2]$.[14, 15] The coexistence of two different dynamics for the M^+ and electron can produce hybrid ion–electron transport materials, which can be utilized for the feature electronic device and the electrode materials of the secondary battery. For instance, the ion transport property combined with the redox behaviors of the metal ions and electrode surface (in a solid state) was used to produce a memristor device in inorganic metal oxide compounds.[43-46] Even in organic materials, ion–electron coupling phenomena have been designed in π-molecular systems bearing crown ether derivatives. Electron-donating crown ether-fused TTF and phthalocyanine (Pc) derivatives have been reported in ion–electron coupling systems,[47-52] while the electron-accepting *p*BQ and *N*-heteroacene derivatives were also hybridized with crown ethers.[53-55] The redox behaviors of crown-ether-fused electron donor and acceptor molecules in the solution phase are affected by the presence of M^+ cations. For instance, the oxidation process of crown-ether-fused TTF generates the cation radical $TTF^{+\bullet}$, where the electrostatic repulsive force between $TTF^{+\bullet}$ and the M^+(crown ether) in the molecule reduces the electron-donating ability of TTF.[49] On the contrary, the reduction process of crown-ether-fused electron acceptor molecules (e.g., *p*BQ) generates anion radical species, where the electrostatic attractive force between M^+(crown ether) and $pBQ^{-\bullet}$ increases the electron accepting ability via M^+ complexation.[55] A chemical design for solid-state M^+ dynamics is difficult to achieve in closest-packing structures. For instance, the formation of ionic channels has been reported in the π-molecular system of crown-ether-fused Pc; this formed a one-dimensional wire array of π-stacking Pc and crown ethers.[47, 28] However, most of the crown ether derivatives fused to the π-molecular system did not form ionic channels. The coupling between the dynamics of M^+ (inside the cavity of the crown ether) and the electronic properties has been reported in the phase transition and dielectric behaviors of M^+(crown ether)$(TCNQ)_x$ crystals.[40-42] The coexistence of a dynamic M^+ environment and redox active structural unit is one possible approach to design the outer stimuli responsible for multifunctional molecular materials.[56-58]

Simple redox-active crown ethers of tetranitoro-dibenzo[18]corwn-6 (**1**) and tetraamino-dibenzo[18]crown-6 (**2**) become electron-accepting and electron-donating molecules (Scheme 1), respectively; these have already been reported as reaction intermediates.[59] However, the redox behaviors, ion complexation ability, crystal structure, and physical properties of **1** and **2** have not been sufficiently examined. The cavity sizes of dibenzo[18]crown-6 (DB18C6) were found to be well fitted to K^+ and to have a high K^+ affinity.[1-3] Depending on the size of M^+, a variety of molecular assembly structures are expected in a combination of M^+ for **1** and **2**. First, we examined the reduction and oxidation behaviors of **1** and **2** in the solution phase; then, single-crystal X-ray structural analyses of M(**1**) complexes for M = Na^+, K^+, Rb^+, and Cs^+ were obtained for the counter cation of I^-, to discuss the complex formation abilities and intermolecular interactions. The electron donor **2** features four proton-accepting $-NH_2$ groups in its molecule; this complicates the redox behavior and crystal structure. Two types of single crystals of $[Na(\mathbf{2})(H_2SO_4)_3]$ and $[K(\mathbf{2})(H_2SO_4)_3]$ were isolated using a complicated crystal formula and hydrogen-bonding networks; furthermore, their dielectric responses and proton conductivity were examined in terms of their responses for H_2O desorption. paragraph text follows directly on here.

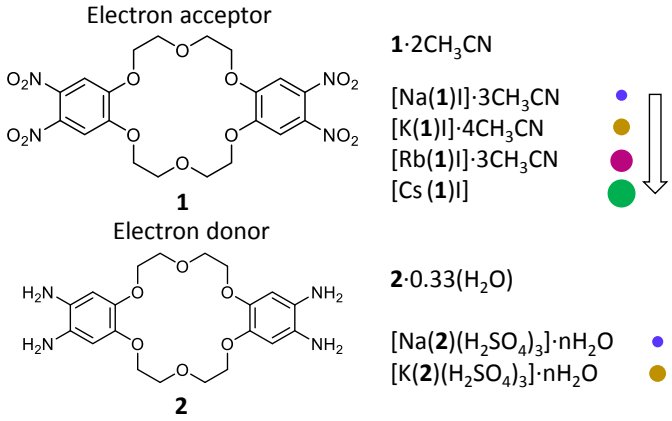

Scheme 1. Molecular structures of the electron-accepting tetranitoro-dibenzo[18]crown-6 (**1**) and electron-donating tetraamino-dibenzo[18]crown-6 (**2**). M^+ complexes of **1** and **2** in this study.

Results and discussion

Redox properties of 1 and 2.

The crown ether derivatives of **1** and **2** are electron acceptor and donor molecules, respectively. Fig. 1 and Table 1 summarize the redox potentials of **1** and **2** in dimethyl sulphoxide (DMSO) (1 mM, vs. SCE) and the effects of 5 equivalent of M^+ addition (Figs. S1 and S2). All other reference compounds of *o*-dinitrobenzene (*o*-DNB), *o*-phenylenediamine (OPD), and TTF were measured at the same condition to those for **1** and **2**. The

This journal is © The Royal Society of Chemistry 20xx

first-wave reduction potential ($E^1_{1/2}$) of **1** was reversibly observed at $E^1_{1/2}$ = −0.780 V, which was ~0.07 V lower than the $E^1_{1/2}$ = −0.706 V observed for *o*-DNB. The introduction of [18]crown-6 into the *o*-DNB unit reduced its electron-accepting ability, which was explained by the electronic effect of the electron-donating –C_2H_4O– units upon the *o*-DNB π-core. The presence of the [18]corwn-6 subunit in molecule **1** can effectively capture alkali metal cations (M^+) in the cavity, which affects the redox behavior via the attractive electrostatic interaction between M^+ and the anion radical state of **1**$^{-\bullet}$. For instance, [18]crown-6 fused *p*BQ derivatives exhibited an anodic shift in $E^1_{1/2}$,[53, 55] where the anion radical state was stabilized by the addition of M via attractive electrostatic interactions. The $E^1_{1/2}$ = −0.780 V of molecule **1** indicated a subtle anodic shift following the addition of Li^+ (ΔE = −11.0 mV), Na^+ (ΔE = −6.0 mV), and K^+ (ΔE = −0.5 mV). Molecule **1** was only soluble in highly polar DMSO or dimethylformamide (DMF), where the formation of M^+(**1**) complexes was restricted in the solution phase without a sufficient value of ΔE for the addition of M+.

Table 1. Redox potentials of **1** and **2** in DMSO.[a]

	E^{ox}, V	E^{red}, V	$E^1_{1/2}$, V	ΔE, mV [b]
1	−0.721	−0.839	−0.780	–
o-DNB	−0.668	−0.745	−0.706	−74.0
1 + Li^+	−0.738	−0.844	−0.791	−11.0
1 + Na^+	−0.731	−0.841	−0.786	−6.0
1 + K^+	−0.734	−0.827	−0.781	−0.5
2	+0.109	+0.039	+0.074	–
OPD	+0.525	–	–	(+416)
TTF	+0.393	+0.326	+0.360	+286
2 + Li^+	+0.112	+0.037	+0.075	+0.5
2 + Na^+	+0.123	+0.042	+0.083	+8.5
2 + K^+	+0.119	+0.047	+0.083	+9.0
[Na(**2**)·(H_2SO_4)$_3$][c]	+0.531	+0.095	+0.313	+239
[K(**2**)·(H_2SO_4)$_3$] [c]	+0.516	+0.122	+0.319	+245

[a] Ligand concentration was fixed at 1 mM and 5 molar M^+ was added for the measurements. [b] ΔE was defined as the difference in the first-wave redox potential $E^1_{1/2}$ between parent **1** or **2** and 10M^+ + **1** or **2** in DMSO. [b] Single-crystals were directly dissolved in the electrode cell for cyclic voltammetry (CV) measurements.

The oxidation process of **2** exhibited complicated behaviors, in contrast to the reduction process of **1**. Molecule **2** acted as both an electron donor and proton acceptor at the OPD units. Fig. 1b shows a possible two-step proton- and electron-transfer scheme for **2**. One OPD unit can accept one proton (H^+) at the –NH_2 group to form mono-protonated $HOPD^+$ cations, whereas the 2H^+ accepting H_2OPD^{2+} dication becomes an unstable chemical species because of the large electrostatic repulsive interaction between the two nearest-neighboring –NH_3^+ groups. The acid dissociation constant (pK_a) of H_2OPD^{2+} has been reported at pK_{a1} = 4.57 and pK_{a2} = 0.80 in H_2O, suggesting an unstable di-protonated state in the solution phase.[60] Therefore, the diagonally di-protonated H_2**2**$^{2+}$ is the most stable and reasonable proton-transferred chemical species for **2**. The electron-donating ability of di-protonated H_2**2**$^{2+}$ differed substantially from that of neutral **2**. Fig. 1c shows the first-wave oxidation potential of **2**, together with the typical electron donors of TTF and OPD. The half-wave first oxidation potential $E^1_{1/2}$ of **2** was observed at +0.074 V; it was +0.286 and +0.416 V stronger than those of TTF and OPD, respectively (lower in Fig. 1c). The reasonably high electron-donating ability of **2** was associated with the effective introduction of two electron-donating –OC_2H_4– units into the OPD π-core. In the DFT calculation based on the B3LYP / 6-31G (d, p) basis set,[61] the energy of the HOMO for OPD (–5.04 eV) was ~0.6 eV lower than that of 4,5-dimethoxy-OPD (–4.40 eV), which was consistent with the difference in $E^1_{1/2}$ values between **2** and OPD. The $E^1_{1/2}$ value of **2** following the addition of Li^+, Na^+, and K^+ indicated almost negligible shifts of ΔE = +0.5, +8.5, and +9.0 mV, respectively.

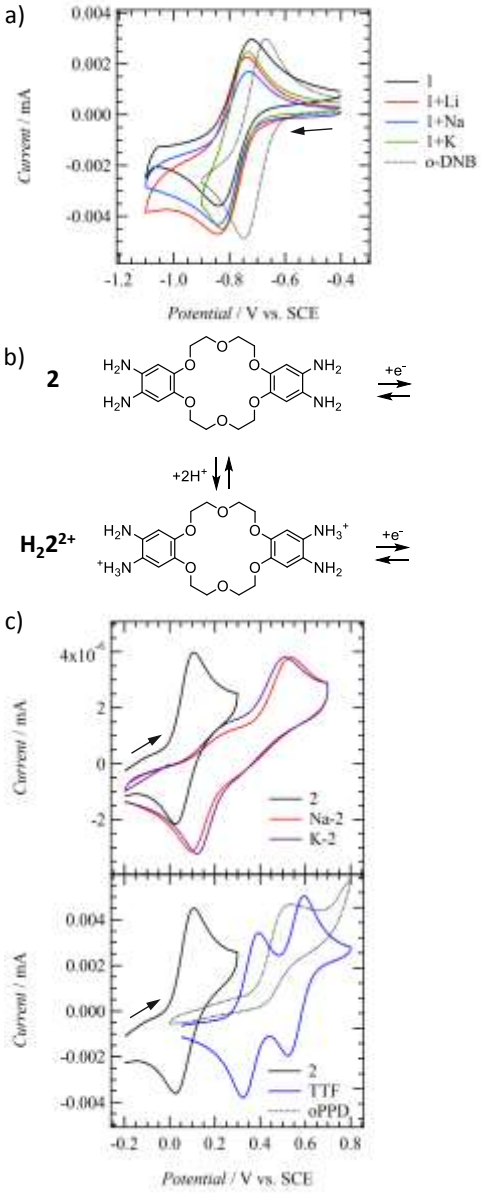

Fig. 1. Redox properties of the electron acceptor **1** and electron donor **2**. a) CV charts of **1** and **1** + M^+ under the addition of 10 molar M^+ of Li^+, Na^+, and K^+ in DMSO (0.1 M TBA•BF_4 vs SCE), along with the CV chart of *o*-DNB. b) The 2H^+ accepting process from the neutral **2** to the di-protonated H_2**2**$^{2+}$. c) The electron donating process of **2**, [Na(**2**)(H_2SO_4)$_3$], and [K(**2**)(H_2SO_4)$_3$] (upper graph), as well as the oxidation processes of typical electron donors of TTF and OPD.

The repulsive electrostatic interaction between $\mathbf{2}^{+\bullet}$ and M^+ reduced the electron-donating ability of **2** following the addition of M^+ in the solution phase. However, dissociation from the M^+(**2**) complex to M^+ + **2** occurred in DMSO during oxidation. We attempted to measure the oxidation behavior of the M^+(**2**) complexes using single-crystals of $[Na(\mathbf{2})(H_2SO_4)_3]\cdot nH_2O$ and $[K(\mathbf{2})(H_2SO_4)_3]\cdot nH_2O$ in DMSO (upper graph in Fig. 1c). The E^{ox} values of $[Na(\mathbf{2})(H_2SO_4)_3]\cdot nH_2O$ and $[K(\mathbf{2})(H_2SO_4)_3]\cdot nH_2O$ were irreversibly observed at almost identical potentials of E^{ox} = +0.531 and +0.516 V, respectively, while the reduction potentials of E^{red} exhibited large anodic shifts to +0.095 and +0.122 V, similar to the E^{red} = +0.039 V for **2**. In DMSO, the presence of acidic HSO_4^- generated an equilibrium between the **2** and $H_2\mathbf{2}^{2+}$ species, and the oxidation of the most stable di-protonated $H_2\mathbf{2}^{2+}$ state was observed in the oxidation process at E^{ox} = +0.52 V. The theoretical energy calculations of HOMOs for OPD, $HOPD^+$, and H_2OPD^{2+} were obtained at −5.04, −11.2, and −15.9 eV, respectively, while those for 4,5-dimethoxy-OPD (DMOPD), $HDMOPD^+$, and H_2DMOPD^{2+} were observed at −4.40, −9.27, and −13.1 eV (Fig. S6). Protonation of the OPD π-core drastically reduced the electron-donating ability. In contrast, the reduction of the di-protonated $H_2\mathbf{2}^{2+}$ state readily occurred in the de-protonation reaction of $H_2\mathbf{2}^{2+} \rightarrow 2H^+ + \mathbf{2}$, which showed an E^{red} value of ~0.10 V for neutral **2**. The protonation and de-protonation processes are associated with the redox behavior of the proton-accepting strong electron donor of **2** in DMSO.

The electronic spectra of **1** and **2** in DMSO showed absorption peaks at 323 and 348 nm, respectively (Figs. 3 and 4). The theoretical HOMO–LUMO energy gap of the isolated molecule **2** (based on DFT calculations) was observed to be ~1.2 eV lower than that of **1**. The addition of 10 M^+ to **2** in DMSO did not change the absorption spectra, suggesting that the presence of excess Na^+ and K^+ cations insufficiently affected the electronic structure of **2**. The high electron-donating ability of **2** resulted in a new electronic absorption band at ~450 nm after 3 days (Fig. S5), which is consistent with the formation of oxidation species in the presence of O_2 and H_2O. The formation of a charge transfer complex between acceptor **1** and donor **2** was not observed upon mixing with DMSO. The addition of a strong electron acceptor, TCNQ, into a solution of **2** in DMSO produced a black solution. However, the solid-state charge transfer complex was not isolated, although the anion radical $TCNQ^{-\bullet}$ was observed in the absorption spectra in DMSO following the addition of **2**.

Crystal structure of 1 and its adsorption properties.

Single-crystals of **1**·2CH_3CN were isolated following the recrystallization of **2** from CH_3CN. Figs. 2a and 2b summarizes the crystal structure of **1**·2CH_3CN at 100 K. Molecule **1** produced a butterfly conformation with a dihedral angle of 120° between the two phenyl-rings (Fig. 2b), and the terminal nearest-neighboring $–NO_2$ groups were twisted to avoid steric repulsion. Fig. 2b shows the unit cell of **1**·2CH_3CN viewed along the *a*-axis without a draw of CH_3CN in CPK mode. A central pore of the [18]crown-6 unit was observed in the *bc* plane, and two moles of CH_3CN occupied the space around the array of **1** in this plane. The one-dimensional (1D) zig-zag arrangement of **1** was observed along the *a*-axis (Fig. 2b), where each central pore overlapped the $–OC_2H_4–$ units at the upper and lower molecules, without the formation of ionic channels. Only the van der Waals interaction connecting molecule **1** and CH_3CN adsorption–desorption behavior was not confirmed in the adsorption–desorption isotherm at 298 K.

CH_3CN molecules in the crystal lattice were gradually eliminated at 298 K under ambient conditions. Thermal annealing at 373 K under vacuum conditions formed desolvated **1** (Fig. S7), which was used for gas (CO_2 and N_2) and molecular (CH_3OH, CH_3CN, and H_2O) adsorption–desorption experiments. The annealed crystal **1** showed Bragg diffraction peaks similar to those of **1**·2CH_3CN, suggesting a crystalline state after the desorption of two molar CH_3CN molecules. Fig. 2c shows the gas adsorption–desorption isotherms of CO_2 at 200 and 298 K and N_2 at 78 and 298 K, respectively. The gate-opened adsorption behavior of CO_2 was observed in the adsorption–desorption isotherm at 200 K, where a significantly low relative pressure of P/P_0 ~ 0 at 200 K opened the CO_2 adsorption crystalline environment to an adsorption quantity of n_{mol} = 1.0 mol mol^{-1}. In contrast, half the level of adsorption at n_{mol} = 0.4 mol mol^{-1} was gradually observed at 298 K without the gate-opening behavior. Similarly, gate-opened N_2 adsorption was confirmed at 77 K with n_{mol} = 0.5 mol mol^{-1}, whereas no N_2 adsorption behavior was observed at 298 K. The adsorption amount of CH_3OH gradually increased up to P/P_0 ~ 0.2 and reached n_{mol} = 1.0 mol mol^{-1} at P/P_0 ~ 0.5, while the monotonic n_{mol} enhancement at the crystal surface adsorption process was observed in the adsorption–desorption isotherm of CH_3CN at 298 K and H_2O at 273 and 298 K. The initial crystals of **1**·2CH_3CN were not recovered by the re-adsorption of CH_3CN at 298 K. The polarized CO_2 molecules were well fitted to open the void space of thermally annealed **1** in the presence of CO_2 gas.

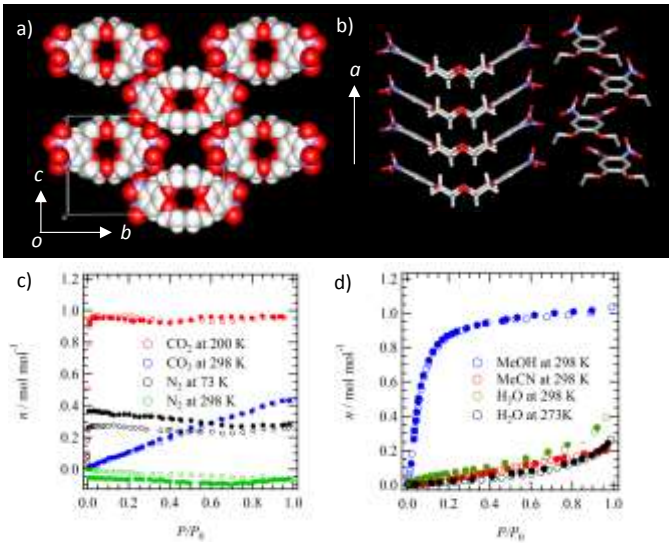

Fig. 2. Crystal structures and adsorption–desorption behavior of **1**·2CH_3CN at 100 K. a) Unit cell viewed along the *a*-axis without the CPK-based representation of CH_3CN molecules. b) Zig-zag stacking arrangement of **1** along the *a*-axis. c) Gas adsorption–desorption isotherm of CO_2 (200 and 298 K) and N_2 (78 and 298 K). d) Molecular adsorption–desorption isotherm of CH_3OH at 298 K, CH_3CN at 298 K, and H_2O at 273 and 298 K.

This journal is © The Royal Society of Chemistry 20xx

Crystal structures of the [M(1)I] salts.

Mixing of **1** with NaI, KI, RbI, and CsI in CH_3CN formed single crystals of [Na(**1**)I]·3CH_3CN, [K(**1**)I]·4CH_3CN, [Rb(**1**)I]·3CH_3CN, and [Cs(**1**)I], respectively (Figs. S8-S11).[62,63] The former three single-crystals (M^+ = Na^+, K^+, and Rb^+) included crystallized CH_3CN molecules in the unit cells; meanwhile, no CH_3CN was observed in the case of Cs^+. Fig. 3 summarizes the crystal structures of [M(**1**)I]·nCH_3CN obtained by changing the M^+ to Na^+, K^+, Rb^+, and Cs^+. All M ions were coordinated by six oxygen atoms inside the cavity of [18]crown-6, where the coordination structure of **1** was influenced by the cation size (Figs 3a–3d). Beside the O6-cooridnaton from the [18]crown-6 unit, the axial –CN coordination of CH_3CN was observed at the M^+ site, with coordination numbers from CH_3CN for Na^+, K^+, Rb^+, and Cs^+ cations of 2, 3, 1, and 0, respectively. The dihedral angles between the terminal two phenyl-rings for Na^+, K^+, Rb^+, and Cs^+ coordination complexes were 123, 124, 139, and 130°, respectively. The average Na^+—O, K^+—O, Rb^+—O, and Cs^+—O distances were observed at 2.69, 2.81, 3.02, and 3.24 Å (Table S3), where the relatively small Na^+ and K^+ cations were well fitted inside the cavity of [18]crown-6 and large size Rb^+ and Cs^+ cations were present at the upper position in the cavity. The Na^+, K^+, Rb^+, and Cs^+ were deviated from the average O6-plane of [18]crown-6 at 0.10, 0.49, 1.22, and 1.67 Å, respectively, according to the ionic radius of Na^+ (1.02 Å), K^+ (1.38 Å), Rb^+ (1.52 Å), and Cs^+ (1.67 Å).

Figs 3e–3h summarizes the unit cells of [M(**1**)I]·nCH_3CN for M^+ = Na^+, K^+, Rb^+, and Cs^+. The O6N2-coordinated [Na(**1**)I]·2CH_3CN units are arranged in the *bc*-plane without effective intermolecular interactions. Only a weak π-overlap at the terminal benzene units was observed along the 1D array along the *c*-axis. One CH_3CN and one I^- anion filled the space between the layers of [Na(**1**)I]·2CH_3CN. The crystal structure of [K(**1**)I]·4CH_3CN resembled that of [Na(**1**)I]·3CH_3CN. The O6N3-coordinated unit of [K(**1**)I]·3CH_3CN was arranged along the *c*-axis with the aid of a weak π-stacking interaction at the terminal benzene units, and CH_3CN and I^- were observed in the space between the layers of [K(**1**)I]·3CH_3CN. In these two crystals, weak van der Waals layers of [M(**1**)I]·nCH_3CN were commonly observed in the π-overlaps of the terminal benzene units. In contrast, a dimer arrangement of {[Rb(**1**)I]·2CH_3CN]}$_2$ was observed in the additional axial O coordination at the Rb^+ site from the $-NO_2$ groups (Fig. 3g).[64, 65] The face-to-face arrangement of two O6N1-coordinated [Rb(**1**)I]·CH_3CN forms a cage-like Rb^+-encapsulated structure. Further increasing the cation size from Rb^+ to Cs^+ generated a 1D coordination polymer along the *b*-axis, where the oxygen atoms of all $–NO_2$ groups were coordinated to Cs^+ cations, forming a 1D Cs^+-coordination polymer (Fig. 3h). Between the 1D polymer chains, effective intermolecular interactions were not observed along the *c*-axis. The M-coordination environments for Na^+, K^+, Rb^+, and Cs^+ were observed in the O6N2, O6N3, O6N1(O2), and O6(O4) structures, respectively, where the latter two large cations of Rb^+ and Cs^+ were coordinated by the oxygen atoms of the $–NO_2$ groups.

Crystal structures of 2 and [M(2)(H_2SO_4)$_3$]·nH_2O.

Fig. 4 shows the crystal structure of **2**·0.33H_2O at 100 K, where three crystallographically independent **2** and 0.33 molar H_2O were observed in the unit cell. The butterfly shaped conformation of **2**, with a dihedral angle of 135° between the two terminal benzene units, resembled that found in **1**. Fig. 4a shows the unit cell of **2**·0.33H_2O, as viewed along the *b*-axis. The central pores of the [18]crown-6 unit were orthogonally arranged along the *b*-axis. Therefore, no ionic channel was observed in the crystal structure of **2**. One H_2O molecule per

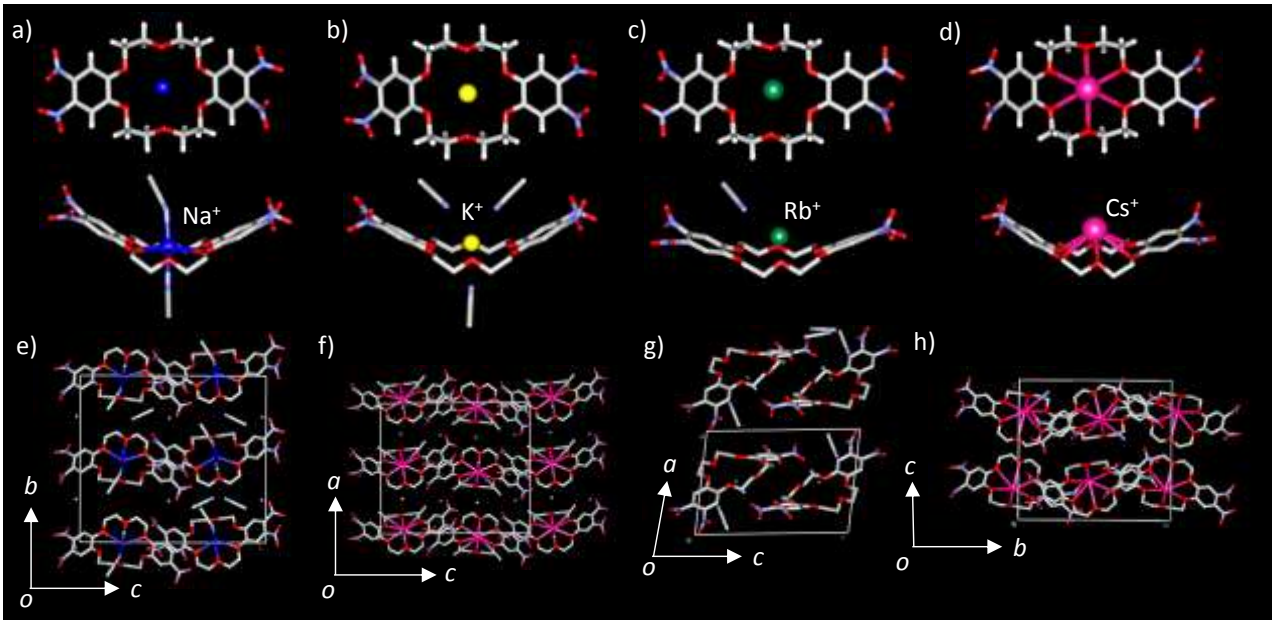

Fig. 3. Crystal structures of [M(**1**)I]·nCH_3CN. Coordination structures and conformations of a) [Na(**1**)I]·2CH_3CN, b) [K(**1**)I]·3CH_3CN, c) [Rb(**1**)I]·CH_3CN, and d) [Cs(**1**)I]. Unit cells of e) [Na(**1**)I]·2CH_3CN viewed along the *a*-axis, f) [K(**1**)I]·4CH_3CN viewed along the *b*-axis, g) [Rb(**1**)I]·3CH_3CN viewed along the *b*-axis, and h) [Cs(**1**)I] viewed along the *a*-axis.

three **2** molecules was occupied in the crystal space, to maintain the closest-packing structure.

Single-crystals of $[Na(\mathbf{2})(H_2SO_4)_3]\cdot nH_2O$ and $[K(\mathbf{2})(H_2SO_4)_3]\cdot nH_2O$ were obtained via a two-phase diffusion method using CH_3OH in the presence of **2** + NaI (or KI) in a diluted H_2SO_4 solution. It was difficult to produce high-quality single-crystals using other combinations of inorganic salts for **2**. The formulas and protonated states of these two single-crystals differed from the simple formula of $[Na(\mathbf{2})(H_2SO_4)_3]\cdot nH_2O$ and $[K(\mathbf{2})(H_2SO_4)_3]\cdot nH_2O$, where the proton-transferred $H_2\mathbf{2}^{2+}$ species and disordered H_2O molecules are present in the single-crystals (Fig. S12). We assumed a possible single-crystal formula based on the charge compensation requirement derived from single-crystal X-ray structural analyses, X-ray photoelectron spectroscopy (XPS) spectra, and elemental analyses. To compensate for the charge valance of single-crystals, di-protonated $H_2\mathbf{2}^{2+}$ species should be present in the crystal formula under acidic crystallization conditions; this provides one possible chemical formula of $[Na^+(H_2\mathbf{2}^{2+})(HSO_4^-)_3]\cdot nH_2O$. However, both elemental analysis and XPS measurements clarified the elemental ratio of Na : **2** : HSO_4 = 0.25 : 1 : 3 without the fully occupied state of Na^+ inside the cavity of the [18]crown-6 unit.

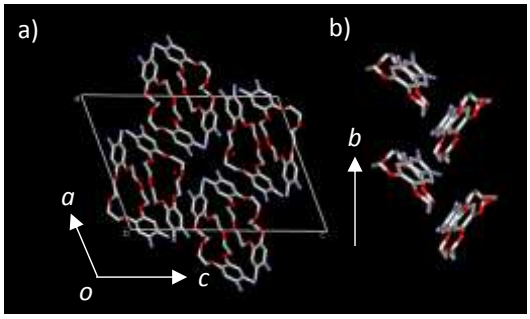

Fig. 4. Crystal structure of **2**·0.33H_2O at 100 K. a) Unit cell viewed along the *b*-axis. b) 1D zig-zag orthogonal array of **2** along the *b*-axis.

Fig. 5a shows the unit cell of $[Na^+(H_2\mathbf{2}^{2+})(HSO_4^-)_3]\cdot nH_2O$ viewed along the *b*-axis. The 1D channel array of **2** was observed along the *b*-axis, and HSO_4^- and H_2O were present around the channel structure of the [18]crown-6 units, where the disordered 6 H_2O molecules occupied the unit cell. Two crystallographically independent **2** molecules and three HSO_4^- anions were observed. From the electron density inside the cavity of two [18]crown-6 units, one cavity was occupied by half of the Na^+ cations, and the second cavity was filled with H_3O^+. The formation of hydronium salts of H_3O^+([18]crown-6)X^- has been reported in previous studies, which revealed the stable H_3O^+ complexation of **2**. Between the ion-capturing units of $(Na^+)_{0.5}(H_2\mathbf{2}^{2+})$ and $(H_3O^+)(H_2\mathbf{2}^{2+})$, the electron density assigned to the other H_2O molecules was observed at the midpoint between the Na^+ and H_3O^+ cations along the *b*-axis and was bridged to the two cations (Fig. 5b). The channel structure was assumed to be $\bullet\bullet\bullet(Na^+)_{0.5}(H_2\mathbf{2}^{2+})\bullet\bullet\bullet H_2O\bullet\bullet\bullet(H_3O^+)(H_2\mathbf{2}^{2+})\bullet\bullet\bullet H_2O\bullet\bullet\bullet$, which is consistent with the molar ratio of Na : **2** = 0.25 : 1 in the XPS spectra and elemental analyses. The total positive charge of +2.75 for $[(Na^+)_{0.25}(H_3O^+)_{0.5}(H_2\mathbf{2}^{2+})]$ unit was compensated by three molar HSO_4^- anions, suggesting that the HSO_4^- anions should be neutral H_2SO_4, to compensate for the total charge valance of the single crystals. Based on these considerations, the single-crystal formula was assumed to be $[(Na^+)_{0.25}(H_3O^+)_{0.5}(H_2\mathbf{2}^{2+})(HSO_4^-)_{2.75}(H_2SO_4)_{0.25}]$, which is consistent with the occupation factor of Na^+ in the single-crystal X-ray structural analysis at 100 K, elemental analysis, and XPS measurements. The mixed protonated state of $(HSO_4^-)_x(H_2SO_4)_{1-x}$ was observed in single-crystals of $[(Na^+)_{0.25}(H_3O^+)_{0.5}(H_2\mathbf{2}^{2+})(HSO_4^-)_{2.75}(H_2SO_4)_{0.25}]$. The ionic channels of $(H_2\mathbf{2}^{2+})_\infty$ interacted with the intermolecular $-NH_3^+\bullet\bullet\bullet O=$ and $-NH_2\bullet\bullet\bullet H-O$ hydrogen-bonding interactions between $H_2\mathbf{2}^{2+}$ and HSO_4^- or H_2SO_4 along the *b*-axis, the hydrogen-bonding structures of which were not clearly confirmed by structural analysis. The existence of six types of crystallographically independent HSO_4^- species in the unit cell complicated the hydrogen-bonding arrangements between HSO_4^- anions and $H_2\mathbf{2}^{2+}$ in the *ab* plane (Fig. S13), where the disordered H_2O molecules also occupied the crystal space between the hydrogen-bonding networks.

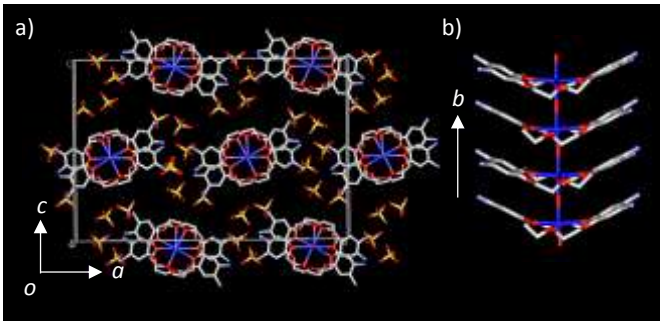

Fig. 5. Crystal structure of $[(Na^+)_{0.25}(H_3O^+)_{0.5}(H_2\mathbf{2}^{2+})\bullet(HSO_4^-)_{2.75}(H_2SO_4)_{0.25}]$ at 100 K. a) Unit cell viewed along the *a*-axis. b) 1D array of $\bullet\bullet\bullet(Na^+)_{0.5}(H_2\mathbf{2}^{2+})\bullet\bullet\bullet H_2O\bullet\bullet\bullet(H_3O^+)(H_2\mathbf{2}^{2+})\bullet\bullet\bullet H_2O\bullet\bullet\bullet\bullet\bullet(Na^+)_{0.5}(\mathbf{2})\bullet\bullet\bullet H_2O\bullet\bullet\bullet H_3O^+(\mathbf{2})\bullet\bullet\bullet H_2O\bullet\bullet\bullet$ along the *b*-axis.

The crystal structure of $[K^+(H_2\mathbf{2}^{2+})(HSO_4^-)_3]\cdot nH_2O$ simple, in contrast to that of $[(Na^+)_{0.25}(H_3O^+)_{0.5}(H_2\mathbf{2}^{2+})(HSO_4^-)_{2.75}(H_2SO_4)_{0.25}]$. One K^+, one $H_2\mathbf{2}^{2+}$, three HSO_4^-, and four H_2O molecules form crystallographically independent structural units in the unit cell of $[K^+(H_2\mathbf{2}^{2+})(HSO_4^-)_3]\cdot 4H_2O$. Figs. 6a and 6b show the unit cells of $[K^+(H_2\mathbf{2}^{2+})(HSO_4^-)_3]\cdot nH_2O$ viewed along the *a*- and *b*-axes, respectively. The channel structure of the $H_2\mathbf{2}^{2+}$ array was not observed, and tight K^+ complexation in the cavity of the [18]crown-6 unit was observed at $d_{K\text{-}O}$ = 2.78 Å. In addition, one H_2O and two oxygen atoms of HSO_4^- were axially coordinated to the K^+ site at $d_{K\text{-}O}$ = 2.70 and $d_{K\text{-}O}$ = 2.86 Å, respectively, forming in the O9-coordination environment at the K^+ cation. The XPS spectra were also consistent with the ratio of K : **2** : HSO_4^- = 1 : 1 : 3, which is likewise consistent with the formula of the single-crystal X-ray structural analysis. Therefore, the charged state of $[K^+(H_2\mathbf{2}^{2+})(HSO_4^-)_3]\cdot 4H_2O$ is the most reasonable crystal formula, which differs substantially from the

This journal is © The Royal Society of Chemistry 20xx

Please do not adjust margins

mixed protonated single-crystals of $[(Na^+)_{0.25}(H_3O^+)_{0.5}(H_2\mathbf{2}^{2+})(HSO_4^-)_{2.75}(H_2SO_4)_{0.25}]$. Slight modulation of the cation size from Na^+ to K^+ drastically altered the M^+-coordination environment and packing structure. The coordinated structures of $[K^+(H_2\mathbf{2}^{2+})(HSO_4^-)_3]$ interacted weakly with the π-stacking interaction at the terminal benzene units and the N–H•••O= and N–H^+•••O= hydrogen-bonding interactions between the terminal and NH_2 and –NH_3^+ groups of $H_2\mathbf{2}^{2+}$ and the other two HSO_4^- anions along the *c*-axis (Fig. 6b). H_2O molecules are present in the space between the hydrogen-bonding networks in the *ac*-plane. The 1D hydrogen-bonding chain of $(HSO_4^-)_\infty$ was elongated along the *c*-axis via K^+ coordinated HSO_4^-, and the O–H•••O= hydrogen-bonding interaction between HSO_4^- anions was also observed along the *b*-axis. The two-dimensional (2D) hydrogen-bonding network was extended in the *bc*-plane.

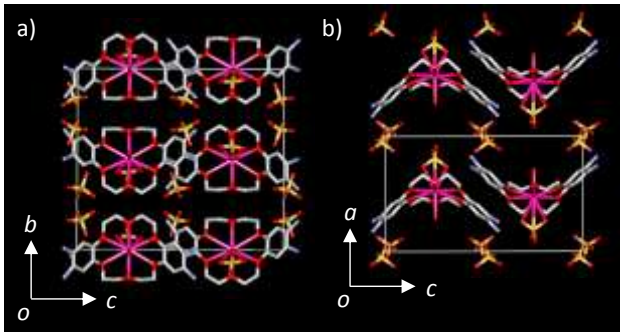

Fig. 6. Crystal structure of $[K^+(H_2\mathbf{2}^{2+})(HSO_4^-)_3]\cdot 4H_2O$ at 100 K. Unit cells a) viewed along the *a*-axis and b) along the *b*-axis. Both H_2O and I^- were omitted for clarity.

Dielectric behavior and proton conductivity.

The temperature (*T*) and frequency (*f*) dependent dielectric responses were evaluated in hydrated crystals of $[M(\mathbf{2})(H_2SO_4)_3]\cdot nH_2O$ and dehydrated $[M(\mathbf{2})(H_2SO_4)_3]$ for M^+ = Na^+ and K^+ (Figs. S14-S17). The dielectric constants are sensitive to the motional freedom of the polar structural unit and the presence of ionic conductivity in the molecular assembly.[66] A parallel circuit of resistance (*R*) and capacitance (*C*) is utilized for the analyses of proton conductivity. When the system is a perfect insulator, the contribution from *R* component is negligible for the analysis. The proton conductivity is largely influenced by the humidity of measurement condition. Therefore, almost the non-humidity condition under the dry N_2 condition was utilized for the *T*- and *f*-dependent dielectric measurements. The hydrated crystals of $[M(\mathbf{2})(H_2SO_4)_3]\cdot nH_2O$ had multiple motional freedoms of Na^+, K^+, H^+, HSO_4^-, and H_2O; this was responsible for the *T*- and *f*-dependent dielectric constants. The long-range motional freedoms of M^+ and H^+ indicate their ionic and protonic conductivities, respectively. Figs. 7a and 7b show the imaginary component dielectric constant (ε_2) of $[(Na^+)_{0.25}(H_3O^+)_{0.5}(H_2\mathbf{2}^{2+})(HSO_4^-)_{2.75}(H_2SO_4)_{0.25}]\cdot 6H_2O$ and dehydrated $[(Na^+)_{0.25}(H_3O^+)_{0.5}(H_2\mathbf{2}^{2+})(HSO_4^-)_{2.75}(H_2SO_4)_{0.25}]$ on the compressed pellets. The dehydrated sample was covered with an epoxy rinse to prevent H_2O adsorption during dielectric measurement. The ε_2 value corresponds to the dielectric loss from the contribution of the conductivity. The appearance of the *T*- and *f*-dependent ε_2 peaks was consistent with the motional freedom in the hydrated crystals of $[(Na^+)_{0.25}(H_3O^+)_{0.5}(H_2\mathbf{2}^{2+})(HSO_4^-)_{2.75}(H_2SO_4)_{0.25}]\cdot 6H_2O$, where ε_2 peaks at *f* = 100 and 316 Hz were observed at 260 and 300 K, respectively. The absolute ε_2 values at 300 K reached ε_2 = 740 for 1 kHz and ε_2 = 330 for 10 kHz. In contrast, monotonic ε_2 enhancement up to 400 K was observed at low-*f* measurement conditions for the dehydrated crystals of $[(Na^+)_{0.25}(H_3O^+)_{0.5}(H_2\mathbf{2}^{2+})(HSO_4^-)_{2.75}(H_2SO_4)_{0.25}]$, where the ε_2 values at *f* = 1 and 10 kHz were observed at ε_2 = 11 and ε_2 = 3, respectively; these were approximately two orders of magnitude smaller than those of the hydrated crystals. The existence of polar H_2O molecules contributed to the poor motional freedom and large dielectric loss of ionic conductivity. In the crystal structure of $[(Na^+)_{0.25}(H_3O^+)_{0.5}(H_2\mathbf{2}^{2+})(HSO_4^-)_{2.75}(H_2SO_4)_{0.25}]\cdot 6H_2O$, the cation of Na^+ was present inside the cavity of the [18]crown-6 unit bridge formed by axial H_2O molecules, which was in accordance with the insufficient Na^+ conductivity in the bulk. However, the 2D hydrogen-bonding network of mixed protonated acidic $(HSO_4^-)_{2.75}(H_2SO_4)_{0.25}$, aided by H_2O molecules, can contribute to the H^+ conductivity (σ_{H+}). Therefore, the presence of σ_{H+} resulted in dielectric loss under the low-*f* measurement condition.

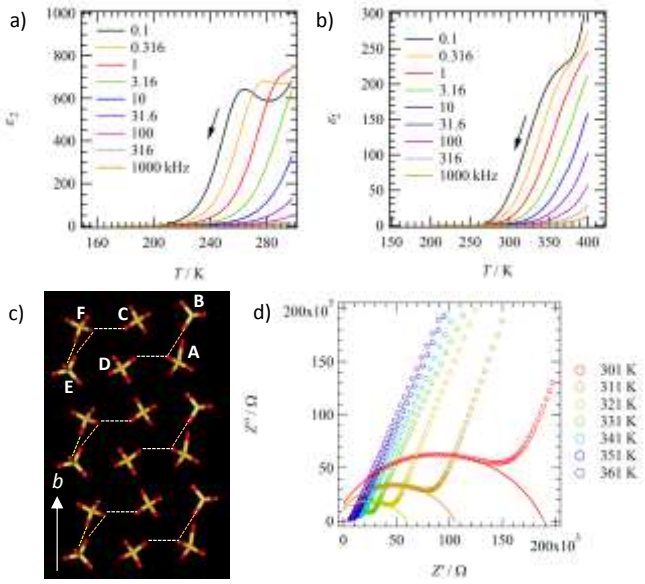

Fig. 7. *T*- and *f*-dependent dielectric responses and proton-conducting behavior of $[(Na^+)_{0.25}(H_3O^+)_{0.5}(H_2\mathbf{2}^{2+})(HSO_4^-)_{2.75}(H_2SO_4)_{0.25}]\cdot 6H_2O$. The ε_2 responses of the a) hydrated and b) dehydrated crystals. c) Hydrogen-bonding network of HSO_4^- and H_2SO_4 along the *b*-axis, where six species of **A**, **B**, **C**, **D**, **E**, and **F** were the independent molecules. d) *T*-dependent Cole–Cole plots of the hydrated crystals on the compressed pellets covered by epoxy rinse.

Fig. 7c shows the O–H•••O= hydrogen-bonding network of HSO_4^- and H_2SO_4 along the *b*-axis, where anionic HSO_4^- and neutral H_2SO_4 coexisted in the network via the hydrogen-bonding interactions of –NH_2 and –NH_3^+ groups at $H_2\mathbf{2}^{2+}$ and H_2O. The complicated hydrogen-bonding network and presence

of H^+ carriers indicate the σ_{H+} value for the hydrated crystals of $[(Na^+)_{0.25}(H_3O^+)_{0.5}(H_2\mathbf{2}^{2+})(HSO_4^-)_{2.75}(H_2SO_4)_{0.25}]\cdot 6H_2O$.

Fig. 7d shows the *T*-dependent Cole–Cole plots for the evaluation of σ_{H+} values. The σ_{H+} = 2.23 μS cm^{-1} at 299 K increased up to 15.4 μS cm^{-1} at 341 K. The *T*-dependent σ_{H+} values followed an Arrhenius plot, and the activation energy (E_a) was obtained at 640 meV for a typical proton-conducting material (Fig. S14). The E_a of nafion films were obtained at ~360 meV (240~298 K) and ~670 meV (140~240 K), where the liquid- and solid-like H_2O molecules played an important role to decide the E_a values.[67] The E_a value of $[(Na^+)_{0.25}(H_3O^+)_{0.5}(H_2\mathbf{2}^{2+})(HSO_4^-)_{2.75}(H_2SO_4)_{0.25}]\cdot 6H_2O$ was similar to that of low-*T* nafion film, suggesting in the less mobile H_2O environment. After the complete dehydration of $[(Na^+)_{0.25}(H_3O^+)_{0.5}(H_2\mathbf{2}^{2+})(HSO_4^-)_{2.75}(H_2SO_4)_{0.25}]$, the magnitude of the dielectric loss was suppressed without proton-conducting behavior, with no semicircular traces in the Cole–Cole plots (Fig. S15). The participation of H_2O molecules in the hydrogen-bonding network produced the σ_{H+} value, with the help of a flexible hydrogen-bonding structure for H^+ transport. Complete H_2O removal from the crystals suppressed the H^+ hopping process and the motional freedom of HSO_4^- and H_2SO_4 in the bulk.

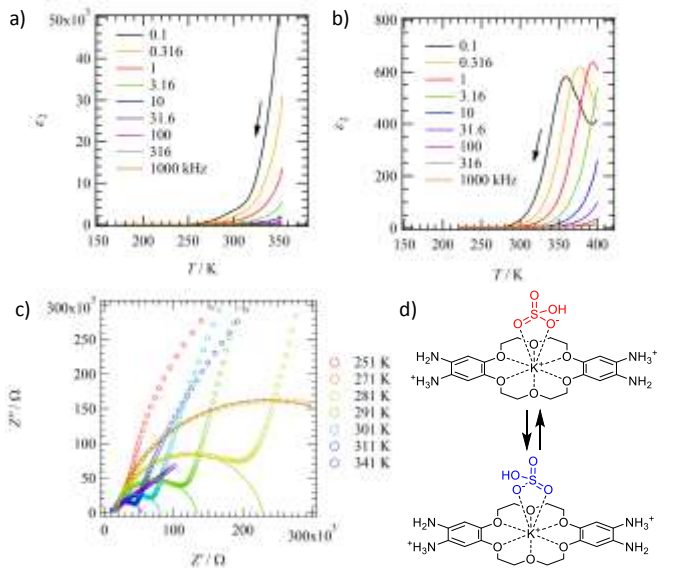

Fig. 8. Motional freedom and dielectric responses of $[K^+(H_2\mathbf{2}^{2+})(HSO_4^-)_3]\cdot 4H_2O$. *T*- and *f*-dependent dielectric responses of a) the hydrated crystals of $[K^+(H_2\mathbf{2}^{2+})(HSO_4^-)_3]\cdot 4H_2O$ and b) the dehydrated crystals of $[K^+(H_2\mathbf{2}^{2+})(HSO_4^-)_3]$. c) *T*-dependent Cole–Cole plots of the hydrated crystals of $[K^+(H_2\mathbf{2}^{2+})(HSO_4^-)_3]\cdot 4H_2O$. d) Schematic images of thermally activated motional freedom for the axially coordinated HSO_4^- anion at the K^+ site.

Figs 8a and 8b show the *T*- and *f*-dependent ε_2 responses of hydrated $[K^+(H_2\mathbf{2}^{2+})(HSO_4^-)_3]\cdot 4H_2O$ and dehydrated $[K^+(H_2\mathbf{2}^{2+})(HSO_4^-)_3]$, respectively. The ε_2 values of the former crystals were approximately two orders of magnitude higher than those of the latter. At a fixed *f*-value of 100 Hz, ε_2 = 55000 at 350 K for hydrated $[K^+(H_2\mathbf{2}^{2+})(HSO_4^-)_3]4\cdot H_2O$ was much larger than the ε_2 = 580 at 350 K for dehydrated $[K^+(H_2\mathbf{2}^{2+})(HSO_4^-)_3]$. The 2D hydrogen-bonding network of HSO_4^- supplemented by H_2O molecules exhibited proton-conducting behavior similar to that of $[(Na^+)_{0.25}(H_3O^+)_{0.5}(H_2\mathbf{2}^{2+})(HSO_4^-)_{2.75}(H_2SO_4)_{0.25}]\cdot 6H_2O$. Fig. 8c summarizes the *T*-dependent Cole–Cole plots of $[K^+(H_2\mathbf{2}^{2+})(HSO_4^-)_3]\cdot 4H_2O$. *T*-dependent semicircular traces were observed in the typical proton-conducting behavior. The E_a = 420 meV (Fig. S16) for $[K^+(H_2\mathbf{2}^{2+})(HSO_4^-)_3]\cdot 4H_2O$ was ~200 meV smaller than that of the hydrated Na^+ salts (E_a = 640 meV), and the σ_{H+} = 22.7 μS cm^{-1} at 341 K for the hydrated $[K^+(H_2\mathbf{2}^{2+})(HSO_4^-)_3]\cdot 4H_2O$ was 1.5 times higher than that of σ_{H+} = 15.4 μS cm^{-1} at 341 K for Na^+ salts. The connectivity and dimensionality of the hydrogen-bonding network of HSO_4^- with the aid of H_2O molecules determines the magnitude and activation energy of the proton-conducting behavior. The redox active and proton conducting MOF and ionic framework have been prepared for the application of proton – electron hybrid conducing electrode materials.[68,69] After H_2O removal from the hydrated crystals of $[K^+(H_2\mathbf{2}^{2+})(HSO_4^-)_3]\cdot 4H_2O$, the proton-conducting pathway was limited to reduce the σ_{H+} value to below 1.96 μS cm^{-1}, whilst Debye-type dielectric relaxation was observed in the *f*-dependent ε_2 peaks in the ε_2–*T* plots of $[K^+(\mathbf{2})(HSO_4^-)_3]$ (Fig. 8b). The ε_2 peaks at *f* = 0.1, 0.316, and 1 kHz shifted to 360, 378, and 393 K, respectively (Fig. 8b). Motional freedom in the dehydrated crystals of $[K^+(H_2\mathbf{2}^{2+})(HSO_4^-)_3]$ was observed under the thermally activated fluctuation of the polar HSO_4^-, where the two types of HSO_4^- anions were present at the axially coordinated site (Fig. 8d) to the K^+ cation and the hydrogen-bonded HSO_4^- around the $[K^+(\mathbf{2})(HSO_4^-)]$ units. Distinguishing between these two motions was difficult in terms of the dielectric responses. However, the suppression of the σ_{H+} values realized motional freedom of polar HSO_4^- in the dehydrated crystals. The thermally activated fluctuation for HSO_4^- anions was observed at E_a = 545 meV (Fig. S17), which was ~100 meV larger than the E_a value of the proton conductivity.

Conclusions

The electron-accepting $-NO_2$ and electron-donating $-NH_2$ groups were introduced into the ion-recognized dibenzo[18]crown-6 (DB18C6), forming a weak electron acceptor, tetranitro-DB18C6 (**1**), and a strong electron donor, tetraamino-DB18C6 (**2**). The electron donating ability of **2** was ~0.29 V larger than that of the typical electron donor of TTF. Effective modulation of the redox behavior was not observed in **1** and **2** under the addition of Li^+, Na^+, and K^+ in DMSO, suggesting insufficient ion recognition inside the cavity of DB18C6. Single crystals of $[M(\mathbf{1})I]\cdot nCH_3CN$ revealed M^+-dependent molecular and packing structures. The crystal structure of $[Rb(\mathbf{1})I]\cdot 3CH_3CN$ was constructed from the cage-like dimer structure of $[Rb(\mathbf{1})I]\cdot 2CH_3CN$, whilst the crystal structure of $[Cs(\mathbf{1})I]$ formed a 1D coordination polymer via effective axial $NO_2\bullet\bullet\bullet Cs^+$ coordination. Electron donor **2** simultaneously realized proton-accepting abilities; it readily generated the di-protonated $H_2\mathbf{2}^{2+}$ state under acidic conditions. The electron donating ability of the di-protonated $H_2\mathbf{2}^{2+}$ was ~0.24 V lower than that of the neutral **2**. Single-crystals of $[(Na^+)_{0.25}(H_3O^+)_{0.5}(H_2\mathbf{2}^{2+})(HSO_4^-)_{2.75}(H_2SO_4)_{0.25}]\cdot 6H_2O$ and

This journal is © The Royal Society of Chemistry 20xx

$[K^+(H_2\mathbf{2}^{2+})(HSO_4^-)_3]\cdot 4H_2O$ were isolated (via crystallization) from a diluted H_2SO_4 solution. The former Na^+ crystals generated the ionic channel of $\bullet\bullet\bullet(Na^+)_{0.5}(H_2\mathbf{2}^{2+})\bullet\bullet\bullet H_2O\bullet\bullet\bullet(H_3O^+)(H_2\mathbf{2}^{2+})\bullet\bullet\bullet H_2O\bullet\bullet\bullet$, as determined by single-crystal X-ray structural analysis, XPS photoelectron spectroscopy, and elemental analysis. The mixed proton-transferred state of $(HSO_4^-)_{2.75}(H_2SO_4)_{0.25}$ was assumed, to compensate for the charge valance of the single-crystals. In contrast, an isolated coordination structure of $[K^+(H_2\mathbf{2}^{2+})(HSO_4^-)]$ was observed in single-crystals of $[K^+(H_2\mathbf{2}^{2+})(HSO_4^-)_3]\cdot 4H_2O$. The two oxygen atoms of the HSO_4^- anion were axially coordinated to the K^+ cation inside the $H_2\mathbf{2}^{2+}$ cavity. In both single-crystals, the anionic HSO_4^- formed an O–H•••O= hydrogen-bonding network with the aid of H_2O molecules; this produced a proton-conducting pathway at a proton conductivity of 23 μS cm^{-1}. However, the dehydration of H_2O molecules suppressed the formation of a suitable proton-conducting hydrogen-bonding network. The simultaneous implementation of redox properties and proton conduction can produce an ion–electron molecular coupling system, a concept that has been observed in biological energy transfer and conversion systems.

Author Contributions

The manuscript was written by TT and TA. All authors have given approval to the final version of the manuscript. YS and HN: all preparations, chemical analyses, CV, optical measurements, single-crystal X-ray analyses, theoretical calculation, and dielectric measurements.

Conflicts of interest

There are no conflicts to declare.

Acknowledgements

This work was supported by a Grant-in-Aid for Scientific Research on KAKENHI (Grant Numbers: JP19H00886, JP20H05865, JP20K05442, and JP20H04655), Japan Science and Technology Agency, Core Research for Evolutional Science and Technology (Grant Number: JPMJCR18I4), and the "Dynamic Alliance for Open Innovation Bridging Human, Environment and Materials" project supported by the Ministry of Education, Culture, Sports, Science and Technology.

Notes and references

1 R. M. Izatt, J. S. Bradshaw, S. A. Nielsen, J. D. Lamb, J. J. Christensen, D. Sen, *Chem. Rev*. 1985, **85**, 271−339.
2 R. M. Izatt, K. Pawlak, J. S. Bradshaw, R. L. Bruening, *Chem. Rev*. 1991, **91**, 1721–2085.
3 G. W. Gokel, I. A. Carasel, *Chem. Soc. Rev*. 2007, **36**, 378–389.
4 G. W. Gokel, W. M. Leevy, M. E. Weber, *Chem. Rev*. 2004, **104**, 2723–2750.
5 J. Li, D. Yim, W. –D. Jang, J. Yoon, *Chem. Soc. Rev*. **2017**, *46*, 2437–2458.
6 S. -P. Zheng, L. -B. Huang, Z. Sun, M. Barboiu, *Angew. Chem. Int. Ed*. 2021, **60**, 566–597.
7 T. Ye, G. Hou, W. Li, C. Wang, K. Yi, N. Liu, J. Liu, S. Huang, J. Gao. *Nature Commun*. 2021, **12**, 5231–1–8.
8 P. L. Anelli, B. Czech, F. Montanari and S. Quici, *J. Am. Chem. Soc*., 1984, **106**, 861–869.
9 F. Nicoli, M. Baroncini, S. Silvi, J. Groppi, A. Credi. *Org. Chem. Front*. 2021, **8**, 5531–5549.
10 M. B. More, D. Ray, P. B. Armentrout, *J. Am. Chem. Soc*. 1999, **121**, 417–423.
11 J. Li, D. Yim, W. –D. Jang, J. Yoon, *Chem. Soc. Rev*. 2017, **46**, 2437–2458.
12 W. Wei, C. Xu, J. Ren, B. Xu, X. Qu, *Chem. Commun*. 2012, **48**, 1284–1286.
13 Y. Nakane, T. Takeda, N. Hoshino, K. –i. Sakai, T. Akutagawa, *J. Mater. Chem. C*. 2017, **5**, 6234−6242.
14 T. Nakamura, T. Akutagawa, K. Honda, A. E. Underhill, A. T. Coomber, R. H. Friend, *Nature*, 1998, **394**, 159–162.
15 T. Akutagawa, T. Hasegawa, T. Nakamura, S. Takeda, T. Inabe, K. Sugiura, Y. Sakata, A. E. Underhill, *Chem. Eur. J*. 2001, **7**, 4902–4912.
16 T. Akutagawa, T. Nakamura. *Coord. Chem. Rev*. 2000, **198**, 297–311.
17 T. Akutagawa, T. Motokizawa, K. Matsuura, S. Nishihara, T, Nakamura. *J. Phys. Chem. B*, 2006, **110**, 5897–5904.
18 T. Akutagawa, T. Hasegawa, T. Nakamura, T. Inabe, T. *J. Am. Chem. Soc*., 2002, **124**, 8903–8911.
19 T. Akutagawa, D. Sato, H. Koshinaka, M. Aonuma, S. –i. Noro, S. Takeda, T. Nakamura. *Inorg. Chem*. 2008, **47**, 5951–5962.
20 T. Akutagawa, A. Hashimoto, S. Nishihara, T. Hasegawa, T. Nakamura, *J. Phys. Chem. B* 2003, **107**, 66–74.
21 Y. –Z. Tang, Y. –M. Yu, J. –B. Xiong, Y. –H. Tan, H. –R. Wen. *J. Am. Chem. Soc*. 2015, **137**, 13345–13351.
22 H. –Y. Ye, Y. Zhang, D. –W. Fu, R. –G. Xiong. *Angew. Chem. Int. Ed*. 2014, **53**, 6724–6729.
23 Y. –F. Zhang, F. –F. Di, P. –F. Li, R. –G. Xiong. *Chem. Eur. J*. 2022, **28**, e202102990–1–10.
24 T. Akutagawa, H. Koshinaka, D. Sato, S. Takeda, S. –i. Noro, H. Takahasi, R. Kumai, Y. Tokura, T. Nakamura, *Nature Materials* 2009, **8**, 342–347.
25 E. C. M. Chen, W. E. Wenthworth, *Mol. Cryst. Liq. Cryst*. 1989, **171**, 271−285.
26 P. Kebarle, S. Chowdhury, *Chem. Rev.* 1987, **87**, 513–534.
27 D. L. Lichtenberger, R. L. Johnston, K. Hinkelmann, T. Suzuki, F. Wudl, *J. Am. Chem. Soc*. 1990, **112**, 3302–3307.
28 K. Seki, *Mol. Cryst. Liq. Cryst*. 1989, **171**, 255–270.
29 U. Geiser, J. A. Schlueter, *Chem. Rev*. 2004, **104**, 5203–5242.
30 J. –Y. Hu, Y. –J. Pu, F. Satoh, S. Kawata, H. Katagiri, H. Sasabe, J. Kido, *Adv. Funct. Mater*. 2014, **24**, 2064–2071.
31 S. V. Rosokha, J. K. Kochi, *Acc. Chem. Res*. 2008, **41**, 641–653.
32 P. J. Henderson, *Annu Rev Microbiol*. 1971, **25**, 393–428.
33 Y. Xu, M. Zhou, Y. Lei, *Materials Today* 2018, **21**, 60–78.
34 A. Rodríguez-Perez, Y. Yuan, C. Bommier, X. Wang, L. Ma, D. P. Leonard, M. M. Lerner, R. G. Carter, T. Wu, P. A. Greaney, J. Lu, X. Ji. *J. Am. Chem. Soc*. 2017, **139**, 13031−13037.
35 S. Dou, S. Zhang, . J. Klein, J. Runt, R. H. Colby, *Chem. Mater*. 2006, **18**, 4288–4295.
36 W. Xu, J. –P. Belieres, C. A. Angell, *Chem. Mater*. 2001, **13**, 575–580.
37 L. Zhang, Z. Zhang, S. Harring, M. Straughan, R. Butorac, Z. Chen, L. Lyons, K. Amine, R. West, *J. Mater. Chem*. 2008, **18**, 3713–3717.
38 A. Nakano, Q. Xie, J. V. Mallen, L. Echegoyen, G. W. Gokel, *J. Am. Chem. Soc*. 1990, **112**, 1287–1289.
39 K. Ichihashi, D. Konno, T. Date, T. Nishimura, K. Y. Maryunina, K. Inoue, T. Nakaya, K. Toyoda, Y. Tatewaki, T. Akutagawa, T. Nakamura, S. Nishihara, *Chem. Mater*. 2018, **30**, 7130–7137.

40 K. Sambe, N. Hoshino, T. Takeda, T. Nakamura, T. Akutagawa, *J. Phys. Chem. C*, 2020, **124**, 13560–13571.
41 K. Sambe, N. Hoshino, T. Takeda, T. Nakamura, T. Akutagawa, *Cryst. Growth Des*. 2020, **20**, 3625–3634.
42 K. Sambe, N. Hoshino, T. Takeda, T. Nakamura, T. Akutagawa, *Cryst. Growth Des.,* 2021, **21***,* 5928–5942.
43 A. Thomas, *Appl. Phys*. 2013, **46,** 093001–1–12.
44 K. Sun, J. Chen, X. Yan, *Adv. Funct. Mater*. 2021, **31**, 2006773–1–33.
45 S. Goswami, S. P. Rath, D. Thompson, S. Hedström, M. Annamalai, R. Pramanick, B. R. Ilic, S. Sarkar, S. Hooda, C. A. Nijhuis, J. Martin, R. S. Williams, S. Goswami, T. Venkatesan, *Nature Nanotech*., 2020, **15**, 380–389.
46 S. H. Jo, T. Chang, I. Ebong, B. B. Bhadviya, P. Mazumder, W. Lu, *Nano Lett*., 2010, **10**, 1297–1301.
47 O. E. Sielcken, M. M. van Tilborg, M. F. M. Roks, R. Hendriks, W. Drenth, R. J. M. Nolte, *J. Am. Chem. Soc*. 1987, **109**, 4261–4265.
48 H. Engelkamp, S. Middelbeek, R. J. M. Nolte, *Science* 1999, **284**, 785–788.
49 M. B. Nielsen, C. Lomholt, J. Becher, *Chem. Soc. Rev*. 2000, **29**, 153–164.
50 T. Akutagawa, T. Ohta, T. Hasegawa, T. Nakamura, C. A. Christensen, J. Becher, *Proc. Nat. Acad. Sci. USA*, 2002, **99**, 5028–5033.
51 T. Akutagawa, K. Kakiuchi, T. Hasegawa, T. Nakamura, C. A. Christensen, J. Becher, *Langmuir* 2004, **20**, 4187–4195.
52 T. Akutagawa, K. Kakiuchi, H. Hasegawa, S. Noro, T. Nakamura, T. Hasegawa, S. Mashiko, J. Becher, *Angew. Chem. Int. Ed.* 2005, **44**, 7283−7287.
53 A. Tsuda, C. Fukumoto, T. Oshima, *J. Am. Chem. Soc*. 2003, **125**, 5811−5822.
54 K. Isoda, H. Takahashi, Y. Mutoh, N. Hoshino, T. Akutagawa, *Dalton Trans*., 2019, **48**, 13125–13129.
55 T. Kobayashi, Y. Nakane, T. Takeda, N. Hoshino, H. Kawai, T. Akutagawa, *Chem. Asian. J*. 2015, **10**, 390–396.
56 T. Akutagawa, *Mater. Chem. Front*. 2018, **2**, 1064–1073.
57 T. Akutagawa, *Bull. Chem. Soc. Jpn*. 2021, **94**, 1400–1420.
58 T. Akutagawa, T. Takeda, N. Hoshino, *Chem. Comm*. 2021, **57**, 8378–8401.
59 S. A. Duggan, G. Fallon, S. J. Langford, V. –L. Lau, J. F. Satchell, M. N. Paddon-Row, *J. Org. Chem*. 2001, **66**, 4419–4426.
60 J. A. Dean, *Handbook of Organic Chemistry*, NY, McGraw-Hill Book Co., 1987.
61 M. J. Frisch, et al., Gaussian 16, Gaussian, Inc. Wallingford CT, 2016.
62 Crystal structure: single crystal structure analysis software. Ver. 3.6, 2004. Rigaku corporation and molecular structure corporation.
63 G. M. Sheldrick, SHELX2014 Programs for Crystal Structure Analysis; Universitat Göttingen: Göttingen, Germany, 2014.
64 A. Hanft, D. Rottschäfer, N. Wieprecht, F. Geist, K. Radacki, C. Lichtenberg, *Chem. Eur. J*. 2021, **27**, 14250–14262.
65 K. M. Fromm, *Coord. Chem. Rev*., 2008, **252**, 856-885.
66 K. C. Kao, *Dielectric Phenomena in Solids*, Elsevier: Amsterdam, 2004.
67 M. Cappadonia, J. . Erning, U. Stimming, *J. Electroanal. Chem*., 1994, **376**, 189–193.
68 D. Bokotial, A. Chowdhury, *Results in Chem*., 2022, **4**, 100361–1–9.
69 N. Ogiwara, T. Iwano, T. Ito, S. Uchida, *Coord. Chem. Rev*., 2022, **462**, 214524–1–13.

This journal is © The Royal Society of Chemistry 20xx